Load–Source Matching With Dielectric Isolation in High-Frequency Switch-Mode Power Supplies

Adrian Zsombor Amanci, *Member, IEEE*, Harry E. Ruda, and Francis P. Dawson, *Fellow, IEEE*

***Abstract*—This paper presents a new hybrid passive power device, denoted as the hybrid transformer, which is an improved alternative to the classical two-winding high-frequency transformer (100's kHz–MHz). The hybrid transformer is comprised of a coupled inductor topology, that provides load–source matching, denoted as the mutual branch topology, and a dielectric isolation device denoted as the multilayer capacitive isolation device. The main focus of this paper is on the design and operation of the mutual branch topology. Simulation results are shown to highlight the improved efficiency of the hybrid transformer over a conventional high-frequency transformer. Finally, the efficiency of the hybrid transformer is compared with that of a classical two-winding transformer using the same resonant converter, highlighting the improved efficiency of the hybrid transformer (up to 10% improved efficiency for light loads).**

***Index Terms*—HF transformers, mutual coupling, power transformer losses, transformer windings.**

I. Introduction

INCREASING the operating frequency of power converters is desirable for the following two reasons: a reduction in the converter footprint and mass, and an increase in the power density of the device [1], [2]. In many cases, a magnetic transformer is used to provide load–source matching and/or galvanic isolation. An unwanted consequence of moving toward higher switching frequencies is a reduction in the efficiency of the magnetic transformers that are employed extensively in power converters. The decrease in the magnetic transformer efficiency is due to: 1) increased winding loss, in the form of skin and proximity effects, and 2) core loss, in the form of eddy currents and hysteresis [3]–[5]. The transformer winding loss can be reduced with the use of Litz wire or copper foil, but results in an increased manufacturing cost. The only material choices for the magnetic core of a high-frequency transformer are ferrites. At frequencies exceeding megahertz, the preferred material choice is a NiZn-based ferrite which has a permeability ranging from (3–20) [6]. Unfortunately, the disadvantages outlined above (winding loss, core loss) remain a limiting issue and are only exacerbated by the higher frequencies of operation (megahertz range) [7], [8].

The two conventional approaches to improve the efficiency of the high-frequency transformer are: 1) changing the transformer layout, or 2) changing the magnetic materials used. The standard layouts of high-frequency transformers are the flat core or racetrack topologies which have the advantage of a lower footprint, while providing similar loss to a regularly wound transformer. The other avenue taken for improving transformer efficiency has been the search for better engineered magnetic materials, while several research groups have reported improvements on different manufactured materials [9], [10], their relative permeability has not been significantly altered. In fact, the operation of many high-frequency magnetic transformers (power loss density and quality factor) does not offer a significant performance increase over air-core transformers [11]. The issues of high losses in the megahertz frequency range remains an ongoing issue for power transformers.

The design alternative proposed in this paper, denoted as the hybrid transformer (HT), is different from most other attempts at improving magnetic transformer performance because it explores the use of a different circuit architecture rather than improving on the design of the classical transformer. The main advantage offered by the proposed HT is a lower input current which results in a higher efficiency when compared to an equivalent classical transformer. The HT is comprised of a pair of coupled air-core windings denoted as the mutual branch topology (MBT), and a dielectric isolation device denoted as the multilayer capacitive isolation device (MLCID). The purpose of the MLCID is to provide galvanic isolation between the source and the load, its design and characterization is presented in a companion paper [12]. The purpose of the MBT is to provide load–source matching with a pair of coupled air-core windings. The HT is the series combination of the MBT and MLCID components.

This paper is organized as follows: Section II presents the MBT's principles of operation together with simulation results that emphasize its advantages over the classical magnetic transformer, while Section III provides an experimental test case comparing the efficiency of an HT and a two-winding magnetic transformer in a resonant power converter. Section IV conclude the paper with a summary of the paper's contents.

II. Operating Principle of MBT

The purpose of the MBTis to provide load–source matching, and its operating principles are the focus of this section.

Manuscript received June 22, 2015; revised November 4, 2015; accepted December 15, 2015. Date of publication December 25, 2015; date of current version May 20, 2016. Recommended for publication by Associate Editor M. A. E. Andersen.

A. Z. Amanci and F. P. Dawson are with the Department of Electrical and Computer Engineering, University of Toronto, Toronto, ON M5S 3G8 Canada (e-mail: zsa.amanci@mail.utoronto.ca; dawson@ece.utoronto.ca).

H. E. Ruda is with the Department of Materials Science and Engineering, University of Toronto, Toronto, Ontario M5S 3G8, Canada (e-mail: harry.ruda@utoronto.ca).

Color versions of one or more of the figures in this paper are available online at http://ieeexplore.ieee.org.

Digital Object Identifier 10.1109/TPEL.2015.2512586

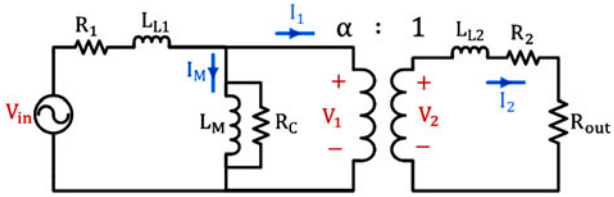

Fig. 1. Electrical circuit representation of a two-winding transformer.

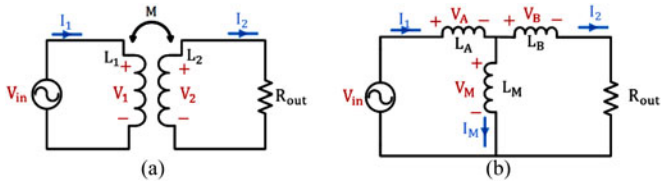

Fig. 2. (a) Coupled model of a two-winding transformer and (b) T-model equivalent representation.

A. Equivalent Electrical Model of the Two-Winding Transformer

Fig. 1 displays the electric circuit model of the classical two-winding transformer with nonidealities included. L_{L1} and L_{L2} represent the leakage inductances of the two windings, R_1 and R_2 are the copper loss associated with the two windings, L_M is the magnetizing inductance branch, and R_c is the core loss. The magnetic designs presented in this paper for both the MBT and the classic two-winding transformer are air-core, hence, the core loss term will be ignored for the remainder of the paper (R_c=0).

The coupled transformer model presented in Fig. 2(a) assumes perfect coupling ($L_{L1} = L_{L2} = 0$) and ignores losses ($R_1 = R_2 = R_c = 0$). The same impedance, current, and voltage transfer functions of the two-winding transformer of Fig. 2(a) can be obtained using the circuit shown in Fig. 2(b). These three component system displayed in Fig. 2(b) is known as a T-model implementation. Note that inductors L_A and L_B are not leakage inductances, they represent standalone components, and as such, the T-model implementation should not be confused with the transformer electrical model representation referred to the primary or secondary sides. To obtain the same transfer functions, the three discrete components of the T-model need to have the following inductance values:

$$L_A = L_1 - M \tag{1}$$

$$L_B = L_2 - M \tag{2}$$

$$L_M = M. \tag{3}$$

Note that if good coupling is assumed ($M \approx \sqrt{L_1 \cdot L_2}$), then L_B will have a negative value for a step-down configuration, and L_A will have a negative value for a step-up configuration. For a practical implementation, the negative inductance component will be realized using a capacitive element.

B. Classical Two-Winding Transformer Equivalent Circuit Model

The analysis of the performance of a two-winding magnetic transformer and a T-model implementation presented in this section will only take into consideration winding losses. The purpose of this analysis is to compare the power loss and the efficiency of a T-model implementation and a two-winding magnetic transformer.

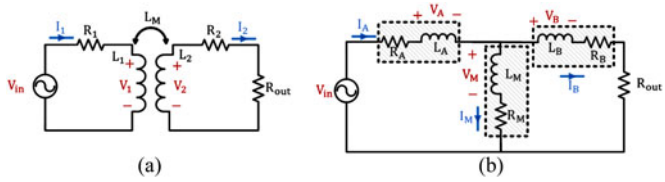

Fig. 3. (a) Two-winding transformer with winding loss and (b) practical T-model implementation represented by individual inductors.

Fig. 3(a) shows the magnetic transformer with winding loss, assuming perfect coupling, while Fig. 3(b) displays the circuit diagram of the physical T-model implementation (the shaded boxes represent individual physical components). The electrical characteristics of the two-winding transformer displayed in Fig. 3(a) can be described with the following equation:

$$\begin{bmatrix} V_{\text{in}} \\ 0 \\ 0 \\ 0 \end{bmatrix} = \begin{bmatrix} -R_1 & 0 & 1 & 0 \\ 0 & -(R_2 + R_{out}) & 0 & 1 \\ j\omega L_1 & j\omega M & -1 & 0 \\ j\omega M & j\omega L_2 & 0 & -1 \end{bmatrix} \cdot \begin{bmatrix} I_1 \\ I_2 \\ V_1 \\ V_2 \end{bmatrix} \tag{4}$$

where the winding resistances R_1 and R_2 and winding self-inductances L_1 and L_2 are determined, based on (5) and (6), respectively

$$L_i = N_i^2 \cdot K_c \tag{5}$$

$$R_i = N_i \cdot R_{\text{MLT}}. \tag{6}$$

The parameter K_c represents the inverse reluctance of the magnetic medium and it is equal to

$$K_c = \frac{\mu_r \mu_0 A_c}{l_c} \tag{7}$$

while R_{MLT} represents the per-turn resistance of the windings, which is assumed to be the same for both windings of the two-winding transformer.

The T-model implementation presented in Fig. 3(b) can be described with the following equation:

$$\begin{bmatrix} V_{\text{in}} \\ 0 \\ 0 \\ 0 \end{bmatrix} = \begin{bmatrix} R_A & R_B & 1 & 1 \\ j\omega L_A & 0 & -1 & 0 \\ 0 & j\omega L_M & 0 & -1 \\ Z_1 & Z_2 & 0 & -1 \end{bmatrix} \cdot \begin{bmatrix} I_A \\ I_M \\ V_A \\ V_M \end{bmatrix} \tag{8}$$

where $Z_1 = j\omega L_B + R_B + R_{\text{out}}$ and $Z_2 = -(j\omega L_B + R_B + R_M + R_{\text{out}})$. The inductance values of the three discrete components (L_A, L_M, L_B) are given by (1)–(3). The resistances of the three components are obtained with the help of (5) and (6)

$$R_i = \sqrt{\frac{L_i}{K_c}} \cdot R_{\text{MLT}} \tag{9}$$

where the index "i" can be replaced with either A, B, or C.

Using the same K_c and R_{MLT} values in (5), (6), and (9) ensures that the resistance associated with each component of the

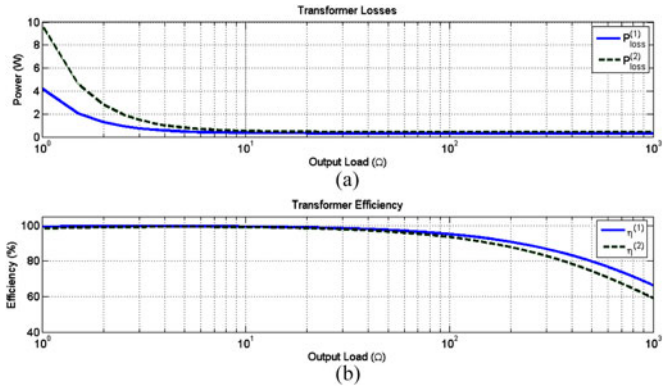

Fig. 4. (a) Simulated power loss and (b) simulated efficiency as a function of output load for the two-winding transformer and the T-model implementation—semilog plots.

TABLE I
SIMULATION PARAMETERS OF THE TWO-WINDING TRANSFORMER AND T-MODEL AT 100 KHZ

Simulation parameters			
$V_{\rm in}$	100-V RMS	f_0	100 kHz
N_1	400	N_2	100
K_c	2.5 nH/turn	$R_{\rm MLT}$	0.05 mΩ/turn
L_1	400 μH	R_1	20 mΩ
L_2	25 μH	R_2	5 mΩ
L_A	300 μH	R_A	17.3 mΩ
L_B	−75 μH	R_B	8.7 mΩ
L_M	100 μH	R_M	10 mΩ

T-model implementation is proportional to the resistance associated with the windings of the magnetic transformer. The total losses of the two-winding transformer [$P_{\rm loss}^{(1)}$] and the practical T-model implementation [$P_{\rm loss}^{(2)}$] can thus be meaningfully compared based on the following two equations:

$$P_{\rm loss}^{(1)} = R_1 \cdot |I_1|^2 + R_2 \cdot |I_2|^2 \tag{10}$$

$$P_{\rm loss}^{(2)} = R_A \cdot |I_A|^2 + R_B \cdot |I_B|^2 + R_M \cdot |I_M|^2. \tag{11}$$

Fig. 4 presents (a) the total losses and (b) the efficiency of the two-winding transformer (solid line), and of the T-model implementation (dashed line), as a function of output load, for the parameters presented in Table I. The losses obtained for the equivalent T-model are consistently larger across the load spectrum, when compared to the two-winding transformer. This is because the total resistance of the three inductors is larger than the total resistance of the two-winding transformer and because of the large current in the parallel inductor branch I_M.

C. Mutual Branch Topology

An implementation of the T-model using discrete components has larger losses than the actual two-winding transformer, as shown in the previous section. However, the T-model implementation can be modified to include mutual coupling between the two inductors in order to reduce losses and increase system efficiency. By selecting an appropriate value of the inductor magnitudes and mutual coupling coefficient, the desired voltage step-up or step-down ratio can be obtained. The circuit

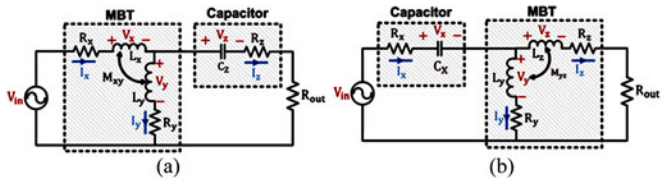

Fig. 5. Circuit diagram for the practical implementation of a (a) step-down MBT and (b) step-up MBT.

TABLE II
SIMULATION PARAMETERS OF THE MBT FOR A 4:1 STEP-DOWN CONFIGURATION AT 100 KHZ

Simulation parameters			
L_x	330 μH	R_x	18.2 mΩ
L_y	40 μH	R_y	6.3 mΩ
$k_{\rm xy}$	0.9	$M_{\rm xy}$	103.4 μH
L_z	−300 μH	R_z	17.3 mΩ

representation of this new proposed model, referred to as the MBT is shown in Fig. 5, and the set of equations describing the behavior of the system is provided below

$$\begin{bmatrix} V_{\rm in} \\ 0 \\ 0 \\ 0 \end{bmatrix} = \begin{bmatrix} R_x & R_y & 1 & 1 \\ j\omega L_x & j\omega M_{\rm xy} & -1 & 0 \\ j\omega M_{\rm xy} & j\omega L_y & 0 & -1 \\ Z_a & Z_b & 0 & -1 \end{bmatrix} \cdot \begin{bmatrix} I_x \\ I_y \\ V_x \\ V_y \end{bmatrix} \tag{12}$$

where $Z_a = j\omega L_z + R_z + R_{\rm out}$ and $Z_b = -(j\omega L_z + R_z + R_y + R_{\rm out})$.

Note that the impedance matrix of (12) is similar to the one shown in (8) that is used to describe the T-model operation. The main difference is the $j\omega M_{\rm xy}$ mutual coupling term which appears in the impedance matrix. Equation (13) shows the expression for the computed MBT power loss

$$P_{\rm loss}^{(3)} = R_x \cdot |I_x|^2 + R_y \cdot |I_y|^2 + R_z \cdot |I_z|^2. \tag{13}$$

The equivalent winding resistance of the three inductors is computed in a similar fashion to the equivalent resistances of the T-model [see (9)].

The MBT parameters displayed in Table II are for a 4:1 step-down implementation at 100 kHz and $R_{\rm MLT}$ is set to be the same as for the two-winding transformer and T-model implementation, whose parameters are shown in Table I.

A load sweep and time domain simulations were performed in order to compare the efficiency of the two-winding transformer, T-model practical implementation, and MBT, using the parameters displayed in Tables I and II. Note that the same inverse reluctance K_c and resistance per mean length turn $R_{\rm MLT}$ is used for all three implementations to ensure a fair comparison.

As seen from Tables I and II, the resistances associated with elements L_x, L_y, and L_z are not lower in magnitude than for the two-winding transformer, which would suggest the MBT total losses equal to, or higher, than the two-winding transformer. However, the efficiency of the two-winding transformer, T-model implementation, and MBT as a function of load shown in Fig. 6 highlights the fact that the MBT provides better efficiency over the two-winding transformer and T-model. The main

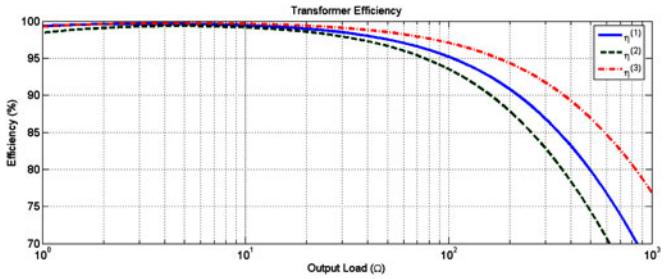

Fig. 6. Simulated efficiencies of the three models as a function of output load: the two-winding model ($\eta^{(1)}$), the T-model ($\eta^{(2)}$) and the MBT ($\eta^{(3)}$)—semilog plot.

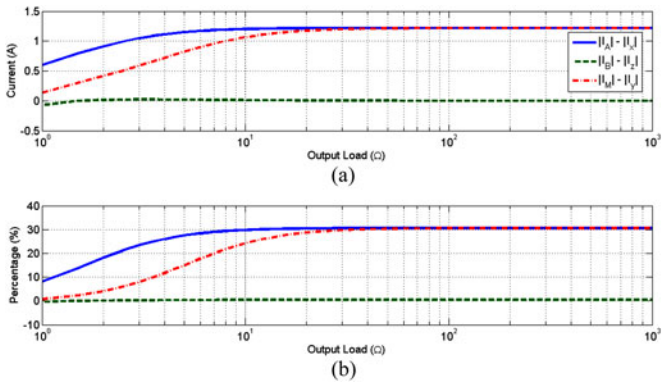

Fig. 7. Simulated difference between the current magnitudes in the T-model and MBT: (a) magnitude and (b) percentage difference; solid line is the difference in input currents, dashed line is the output current difference, and dash-dot line is the parallel branch current difference—semilog plots.

reason for the increased efficiency and decreased total losses of the MBT is the lower input current magnitudes, when compared to the other two models. Fig. 7 highlights this important advantage of the MBT implementation, the magnitude of the currents flowing through the inductor network is lower for the MBT, when compared to the T-model implementation. While efficiencies for large loads are similar for the given parameters, there is a clear advantage of the MBT in terms of losses for light loads (note that the magnitude of the input and parallel branch currents in Fig. 7 are 30% higher for the T-model implementation in comparison with the MBT). The difference in output currents for the MBT and T-model implementation is close to zero (see the dashed line in Fig. 7), as expected. This lower input current is also highlighted with the help of time domain simulations performed with the help of MATLAB Simulink and the SimPowerSystems Library. Fig. 8 displays the plot of the relevant currents for the three discussed models as a function of time for an output load of 2.5 Ω and a sinusoidal voltage source. Observe that the input current for the MBT implementation is slightly lower when compared to the input current of the two-winding transformer and T-model implementation (upper plot of Fig. 8).

Table III displays a new set of parameters for the three different models (two-winding transformer, T-model implementation, and MBT) used for a new set of simulations performed at 5 MHz. Fig. 9 displays the efficiency as a function of load for the three

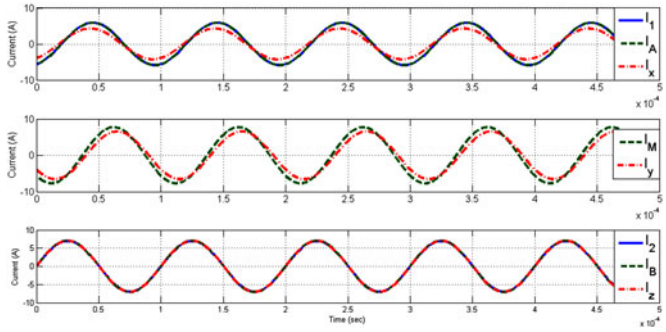

Fig. 8. Time domain simulation of the model currents for a 2.5-Ω load.

TABLE III
SIMULATION PARAMETERS FOR A 4:1 TRANSFORMER AT 5 MHZ

Simulation parameters			
V_{in}	40 V RMS	f_0	5 MHz
N_1	40	N_2	10
K_c	0.25 nH/turn	R_{MLT}	5 mΩ/turn
L_1	400 nH	R_1	200 mΩ
L_2	25 nH	R_2	50 mΩ
L_A	300 nH	R_A	173 mΩ
L_B	−75 nH	R_B	87 mΩ
L_M	100 nH	R_M	100 mΩ
L_x	300 nH	R_x	173 mΩ
L_y	50 nH	R_y	63 mΩ
k_{xy}	0.7	M_{xy}	98.6 nH
L_z	−100 nH	R_z	100 mΩ

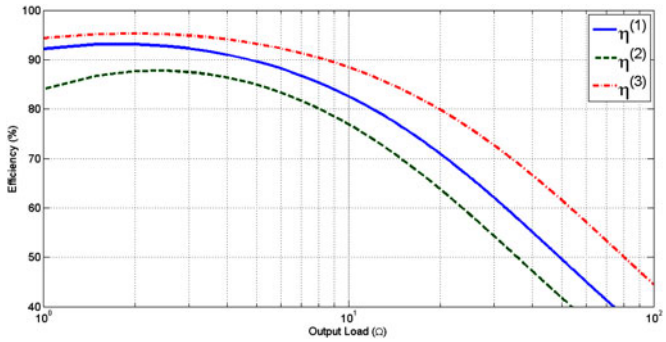

Fig. 9. Simulated efficiency of the 4:1 step-down implementations at 5 MHz as a function of output load—semilog plots.

models operated at 5 MHz. Note that the MBT implementation has higher efficiencies than the two-winding transformer and T-model implementation when operated at higher frequencies (megahertz range).

A MBT step-up configuration can be obtained by switching the input and output terminals of the step-down configuration. The results of a 1:4 step-up configuration simulation are presented in Fig. 10, for the same design parameters outlined in Table III. As with the previous example (see Fig. 9), the MBT has a higher efficiency than the two-winding transformer and T-model implementation, especially for lighter output loads (higher equivalent output resistance).

In summary, the MBT is able to provide higher efficiency for the entire simulated load range (1–100 Ω), when compared to

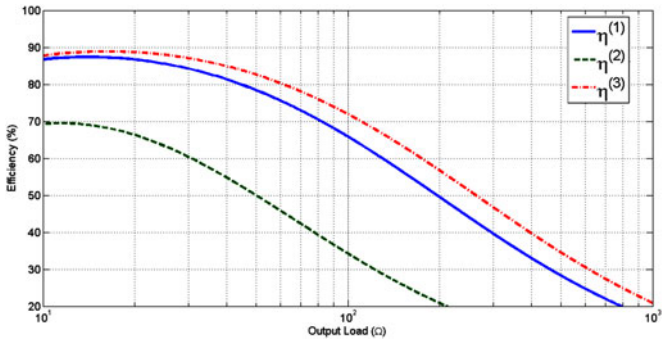

Fig. 10. Simulated efficiency of 1:4 step-up models at 5 MHz as a function of output load.

the two winding transformer, for both the step-up and step-down configurations. The efficiency advantage of the MBT is more pronounced for lighter loads and higher operating frequencies (megahertz rather than 100s of kilohertz range), where simulation results show a disparity as large as 10% between the efficiency of the MBT and two-winding transformer.

III. PCB Air Core Winding Implementation

The implementation of the MBT was chosen to be an air-core toroidal winding topology. A coreless topology was chosen in order to eliminate the core loss dynamics from the head-to-head comparison between the MBT and classical transformer, and because of the high operating frequency (1 MHz). We have opted for windings constructed on a PCB due to the ease of customization available. Thus, air-core PCB windings were constructed by interconnecting the top and bottom traces through hole vias.

The electric and magnetic fields generated within and around the PCB air-core winding were simulated with COMSOL Multiphysics 4.3, a finite element analysis software package. These simulations revealed that the magnetic field is concentrated within the toroidal structure (between the top and bottom PCB traces and between the inner and outer vias), and that the equivalent inductance of the PCB air-core winding is close to the analytically computed value. As an example, Fig. 11(a) and (b) displays the magnetic field lines for a 20-turn, air-core PCB inductor, while Fig. 11(c) displays the normalized magnetic field density for a vertical cross section of the winding. Note that the field is concentrated around the inner radius of the toroid.

To test the PCB air-core windings used for the MBT and two-winding transformer implementations, we have manufactured several windings on a PCB (standalone and mutually coupled windings), as shown in Fig. 12. The purpose of manufacturing PCB air core windings is to compare the theoretical and experimentally measured inductance and resistance values. For both the standalone windings and the MBT configurations, we have built two implementations: one where the outer via radius is equal to the inner via radius, and one where the outer via radius is three times larger than the inner via radius. These two types of implementations were realized in order to test the impact of the copper surface area on the inductance and resistance of the winding.

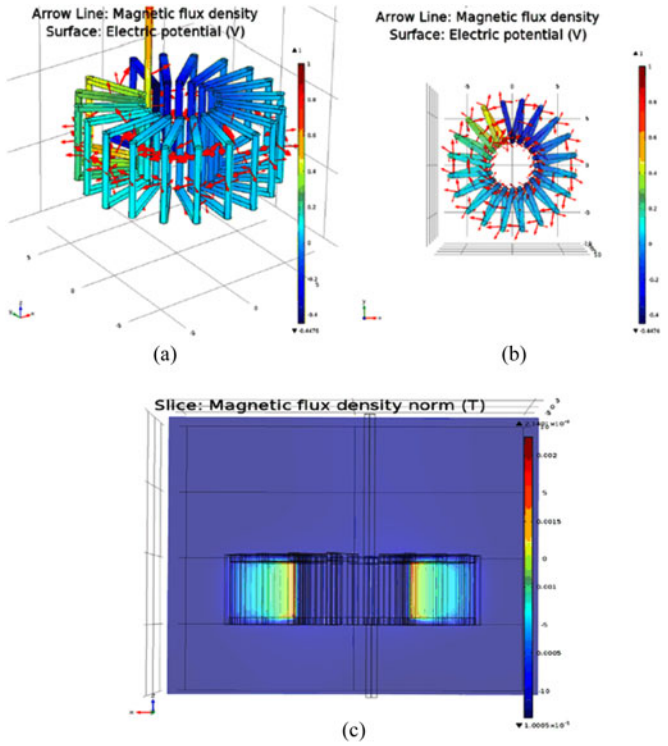

Fig. 11. COMSOL 4.3 simulation results for 20 turn air-core inductor: (a) magnetic field lines—perspective view, (b) magnetic field lines—top view, and (c) normalized magnetic field density—vertical cross section.

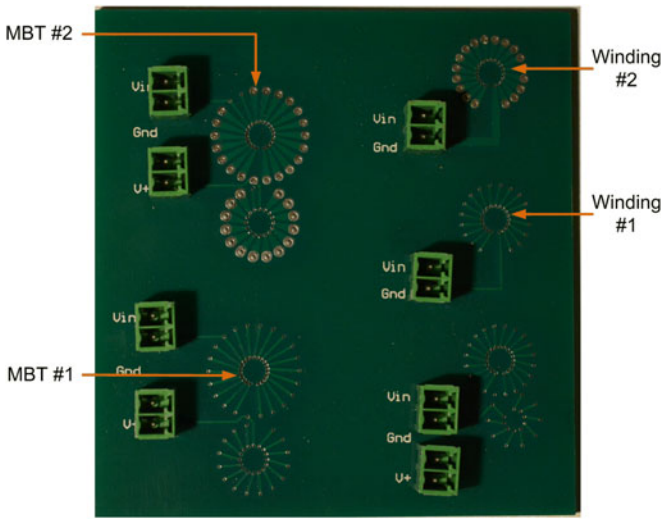

Fig. 12. Single and coupled PCB air-core windings.

For the two standalone windings in Fig. 12 (denoted as Winding #1 and Winding #2), the inductance associated with both windings was estimated to be approximately 230 nH. The equivalent resistance of the windings is estimated with a per turn resistance model (R_{turn}). For Winding #1, the total equivalent resistance is 62 mΩ at 100 kHz and 104 mΩ at 1 MHz. Similarly, for Winding #2, the total resistance is equal to 54 mΩ at 100 kHz and 84 mΩ at 1 MHz, which is a decrease in total resistance by approximately 20 mΩ at 1 MHz.

TABLE IV
MEASUREMENTS FOR TWO STANDALONE AIR-CORE PCB WINDINGS

N=20, r_{in} = 2.5 mm, r_{out} = 6.5 mm				
freq	L_1 nH	R_1 mΩ	L_2	R_2 mΩ
100 kHz	310	80	304	72
400 kHz	306	94	302	86
1 MHz	300	130	300	117
2 MHz	298	163	295	144
10 MHz	305	312	294	291

TABLE V
IMPEDANCE MEASUREMENTS FOR TERMINALS $V_{IN} - V_{GND}$

freq	L_{eq-1}	R_{eq-1}	L_{eq-2}	R_{eq-2} mΩ
100 kHz	582 nH	274 mΩ	612 nH	320 mΩ
400 kHz	558 nH	316 mΩ	600 nH	363 mΩ
1 MHz	542 nH	363 mΩ	589 nH	391 mΩ
2 MHz	536 nH	447 mΩ	577 nH	425 mΩ
10 MHz	544 nH	720 mΩ	586 nH	660 mΩ

Impedance measurements were performed with the help of the 4275A *LCR* meter for the standalone windings shown in Fig. 12. The obtained results are displayed in Table IV. The inductance values recorded with the *LCR* meter are approximately 70–80 nH larger for both the windings. This difference between theoretical and measured inductance is attributed to the inductance introduced by the input/ground traces together with the leads from the input connector to the measurement device (the inductance of a connector and leads was approximately 40–50 nH in a standalone measurement). The reduction in total resistance for Winding #2 is lower than predicted by the per turn model (13 mΩ at 1 MHz instead of 20 mΩ), which suggests that an increase in the outer via radius will have less of an impact on the total winding resistance.

The MBT implementations seen in Fig. 12 (denoted as MBT #1 and MBT #2) are for a 4:1 step-down configuration. The design parameters are: $L_x = 300$ nH, $L_y = 50$ nH, $k_{xy} = 0.7$, where L_x is the series inductor, L_y is the parallel inductor, and k_{xy} is the mutual coupling coefficient between the two windings. We have performed impedance measurements with the *LCR* meter between the V_{in} and V_{gnd} terminals. The expected equivalent measured inductance is equal to

$$L_{eq} = L_x + 2k_{xy}\sqrt{L_x L_y} + L_y \approx 520 \text{ nH}. \quad (14)$$

The experimental measurements are presented in Table V. The measured inductance values are larger than the theoretical values (520 nH) because of the additional inductance associated with the input traces and the connectors, and because of the unaccounted leakage inductance. This is similar to the standalone winding case and is as expected, since the geometry of the connector and connector leads is the same.

The two impedance tests presented in this section for the standalone and mutually coupled windings suggest that there is an agreement between the theoretical impedance values and the experimental results obtained for a given air-core PCB winding configuration.

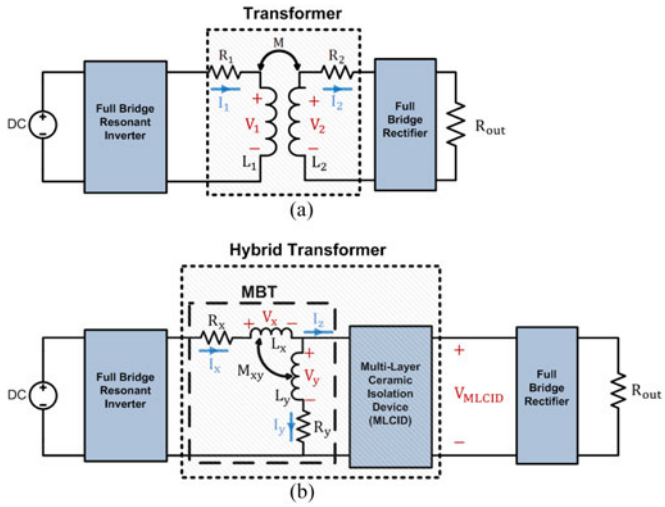

Fig. 13. Diagram of converter with (a) classical transformer and (b) MBT plus MLCID.

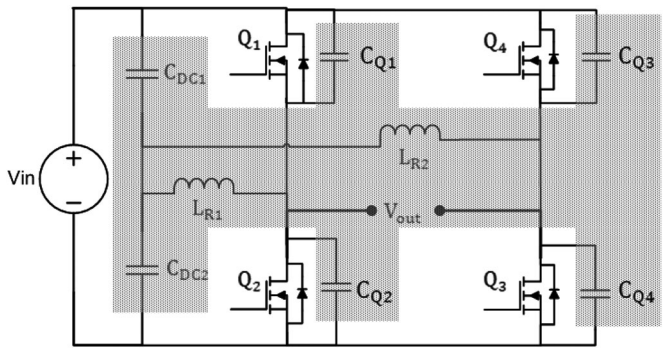

Fig. 14. Full-bridge resonant inverter topology used for the two power converters.

IV. RESONANT CONVERTER IMPLEMENTATION

Experiments were performed to validate the simulation results and highlight the improved efficiency of the HT in comparison to the classical two-winding transformer. Two resonant converters were built on the same PCB, one converter has a two-winding air-core transformer with a 4:1 step-down ratio, while the other converter uses the MBT-MLCID hybrid to provide the required galvanic isolation and 4:1 step-down configuration. Fig. 13 displays the circuit setup for the two resonant converters with (a) two winding magnetic transformer and (b) HT (MBT and MLCID in series). The full-bridge resonant converters are completely identical. This is to ensure that the comparison made between the efficiency of the two winding transformer and the MBT-MLCID hybrid component is fair. The converter with the HT can be separated into three components of interest which will be further detailed: 1) the full-bridge resonant inverter, 2) the MBT, and 3) the MLCID.

A. Full-Bridge Resonant Inverter

The electrical circuit of the full-bridge resonant inverter, for both converters shown in Fig. 13, is displayed in Fig. 14. For the full-bridge inverter comprised of MOSFETs Q1–Q4, zero-voltage switching is achieved with the help of an auxiliary circuit shown

TABLE VI
TOROIDAL AIR-CORE INDUCTOR NETWORK SPECIFICATIONS

Transformer	h_{via}	3.1 mm	L_1	1200 nH
	r_{in}	5 mm	L_2	75 nH
	r_{out}	17.5 mm	M	300 nH
	r_{via}	0.25 mm	R_{MLT}	13.3 mΩ
MBT	h_{via}	3.1 mm	L_x	1000 nH
	r_{in}	5 mm	L_y	110 nH
	r_{out}	17.5 mm	M_{xy}	300 nH
	r_{via}	0.25 mm	R_{MLT}	13.3 mΩ

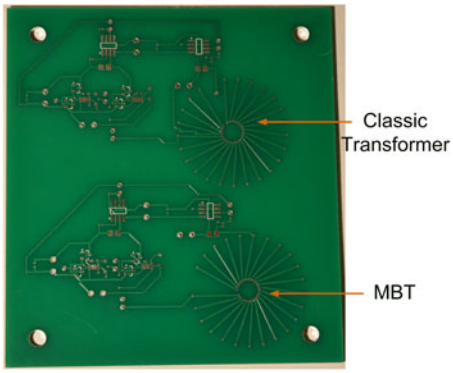

Fig. 15. PCB realization of the full-bridge resonant inverter with the magnetic transformer and the full-bridge resonant inverter with the MBT.

in the shaded regions of Fig. 14. Further details on this resonant converter switching scheme can be found in [13]. The legs of the full-bridge resonant converter were controlled by two half-bridge gate drivers. The half-bridge gate drivers were controlled with phase shifted gating signals generated at 1 MHz, with the help of an Altera DE2 board.

B. MBT Implementation

A classical two-winding transformer and MBT air-core structures were realized by utilizing 3oz copper traces on the bottom and top surfaces of a 3-mm-thick PCB board. Windings were constructed by interconnecting the top and bottom traces with 0.5 mm diameter through hole vias.

The MBT and two-winding transformer specifications for a 4:1 step-down ratio are presented in Table VI; note that all relevant geometrical parameters (height and radius of vias, inner and outer toroidal radii) for the two-winding transformer and MBT are identical to ensure a fair comparison. The PCB of the two converters designed and built is shown in Fig. 15. The two spirals to the right of Fig. 15 are the two-winding transformer and the MBT air-core PCB implementations whose parameters are specified in Table VI. The computed resistance associated with winding L_1 is approximately 540 mΩ, while the resistance associated with L_2 is approximately 150 mΩ (for the two-winding transformer). The resistance associated with winding L_x is equal to 470 mΩ while the resistance associated with L_y is approximately 230 mΩ (for the MBT).

C. MLCID Implementation

The capacitive isolation was realized with the help of a MLCID, which was introduced in a previous paper [12]. The purpose of the MLCID is to provide galvanic isolation at high frequencies through capacitive coupling while achieving high transfer power efficiency. The relevant parameters of the MLCID are shown in Table VII.

TABLE VII
MLCID PARAMETERS

Footprint (mm)	10×10×6.5	Lead radius	2 mm
Electr. (Cr/Au)	50/200 nm	# of plates	20
tanδ (Alum)	0.15%	Alum-ϵ_{low}	9
tanδ (BST)	0.68%	BST-ϵ_{high}	1300
Thickness (BST)	150 μm	Rated voltage	300 V
Thickness (Alum)	500 μm	Rated current	2 A
$\Delta\epsilon_{\text{high}}$ 0–70 °C	15%	V_{break}	1.2 kV

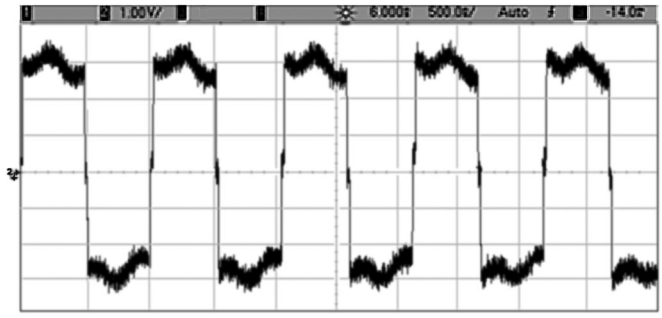

Fig. 16. Voltage at the MLCID output terminals for a 20-Ω load, for the HT implementation; 1 V/div, 500 ns/div.

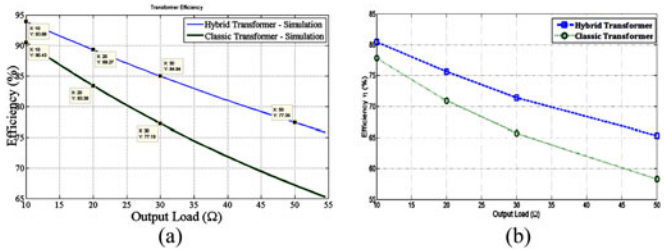

Fig. 17. Efficiency measurements for the classic two-winding transformer and the HT: (a) simulation and (b) experimental results.

D. Efficiency Results

Both converters shown in Fig. 13 run simultaneously at an operating frequency of 1 MHz. Fig. 16 displays the voltage at the MLCID output terminals, for a 12-V dc input with a 20-Ω output load, for the HT implementation. The MLCID output voltage has a magnitude of approximately 3 V, which confirms the 4:1 ratio of the obtained with the MBT-MLCID hybrid component.

Fig. 17(a) displays the simulated efficiency results obtained with the setup parameters, and Fig. 17(b) displays the experimental results. The converters were operated at four different output loads, and the overall converter efficiency was computed for each separate implementation. The experimental efficiencies were obtained by measuring the voltage drop across the output load, computing the output power, and dividing it by the total input power available from the input power supply. Note that the efficiency of the experimental results is lower than the simulation results due to the additional power loss of the

resonant converters and connector leads which were not included in the simulation results. The efficiency of both models drops for increasing resistance because the total power delivered scales inversely with the output resistance, but the power loss of the converter does not.

Also note that while the efficiencies are relatively low for both topologies (mainly due to the increased resistance associated with the copper traces and converter losses), the HT has a better overall efficiency when compared to the two-winding magnetic transformer, especially for lighter loads. As detailed in Section II-C, the increased efficiency is due to the lower magnitude of the input current for the MBT topology when compared to the two-winding transformer.

V. Conclusion

This paper has presented an alternative design to the classical high-frequency transformer denoted as the HT. The HT topology provides load–source matching with the MBT and galvanic isolation with the MLCID. An efficiency comparison was made between the classical two winding transformer and the HT. The simulation results presented show that the HT is able to provide improved efficiency (as large as 2–3% for high load and 10% for low load) over the conventional two-winding high-frequency transformer. This improved efficiency is mainly due to the reduced input current magnitude of the MBT when compared to the two-winding transformer, which becomes even more pronounced as the operating frequency is increased. These simulation results were confirmed experimentally using two identical resonant converters—one operated with the HT, comprised of the MBT and MLCID components, and one operated with the classic two-winding magnetic transformer.

References

[1] D. J. Perreault, H. Jingying , J. M. Rivas, H. Yehui, O. Leitermann, R. C. N. Pilawa-Podgurski, A. Sagneri, and C. R. Sullivan, "Opportunities and challenges in very high frequency power conversion," in *Proc. 24th Annu. IEEE Appl. Power Electron. Conf.*, Washington, DC, USA, Feb. 2009, pp. 1–14.

[2] R. C. N. Pilawa-Podgurski, A. D. Sagneri, J. M. Rivas, D. I. Anderson, and D. J. Perreault, "Very-high-frequency resonant boost converters," *IEEE Trans. Power Electron.*, vol. 24, no. 6, pp. 1654–1665, Jun. 2009.

[3] O. A. Hassan, C. Klumpner, and G. Asher, "Design considerations for core material selection and operating modes for a high frequency transformer used in an isolated DC/DC converter," in *Proc. 14th Eur. Power Electron. Appl. Conf.*, Birmingham, U.K., Aug. 2011, pp. 1–11.

[4] J. Lu and F. Dawson, "Analysis of Eddy current distribution in high frequency coaxial transformer with Faraday shield," *IEEE Trans. Magn.*, vol. 42, no. 10, pp. 3186–3188, Oct. 2006.

[5] W. G. Odendaal and J. A. Ferreira, "A thermal model for high-frequency magnetic components," *IEEE Trans. Ind. Appl.*, vol. 35, no. 4, pp. 924–931, Jul./Aug. 1999.

[6] Y. Han, G. Cheung, A. Li, C. R. Sullivan, and D. J. Perrault, "Evaluation of magnetic materials for very high frequency power applications," *IEEE Trans. Power Electron.*, vol. 27, no. 1, pp. 425–435, Jan. 2012.

[7] S. Yang, S. Abe, and M. Shoyama, "Design consideration of flat transformer in LLC resonant converter for low core loss," in *Proc. Int. Power Electron. Conf.*, Sapporo, Japan, Jun. 2010, pp. 343–348.

[8] J. Zhang, J. Wang, and X. Wu, "A capacitor-isolated LED driver with inherent current balance capability," *IEEE Trans. Ind. Electron.*, vol. 59, no. 4, pp. 1708–1716, Apr. 2012.

[9] Y. Shirakata, N. Hidaka, M. Ishitsuka, A. Teramoto, and T. Ohmi, "High permeability and low loss Ni–Fe composite material for high-frequency applications," *IEEE Trans. Mag.*, vol. 44, no. 9, pp 2100–2106, Sep. 2008.

[10] A. Urata, M. Yamaki, M. Takahashi, K. Okamoto, H. Matsumoto, S. Yoshida, and A. Makino, "Low core loss of non-Si quaternary $Fe_{83.3}B_8P_8Cu_{0.7}$ nanocrystalline alloy with high B_s of 1.7T," *J. Appl. Phys.*, vol. 111, p. 07A335, 2012.

[11] J. Qiu, H. Syed, and C. Sullivan, "Complex permeability measurements of radial-anisotropy thin-film magnetic toroidal cores," *Energy Convers. Congr. Expo.*, Denver, Colorado, Sep. 2013, pp. 1660–1667.

[12] A. Z. Amanci, H. E. Ruda, and F. P. Dawson, "Galvanic isolation for high frequency applications using an integrated dielectric structure," *IEEE Trans. Power Electron.*, vol. PP, no. 99, 2015.

[13] P. K. Jain, W. Kang, H. Soin, and Y. Xi, " Analysis and design considerations of a load and line independent zero voltage switching full bridge DC–DC converter topology," *IEEE Trans. Power Electron.*, vol. 17, no. 5, pp. 649–657, Sep. 2002.

Adrian Zsombor Amanci (M'08) received the B.A.Sc, M.A.Sc, and Ph.D. degrees in electrical engineering from the University of Toronto, Toronto, Canada, in 2007, 2009, and 2014, respectively.

During the Ph.D. degree, he has worked on two different industry sponsored research projects under the supervision of Prof. F. P. Dawson. His research interests include piezoelectric power generation, the development of monitoring and control devices for large scale power systems and high frequency passive power devices.

Dr. Amanci is currently a Post Doctoral Fellow with the University of Toronto.

Harry E. Ruda received the Ph.D. degree from the Massachusetts Institute of Technology, Cambridge, MA, USA, in 1982.

From 1982 to 1984, he was an IBM Postdoctoral Fellow and developed one of the first theories for electron transport in selectively doped 2-D electron gas heterostructures. From 1984 to 1989, he was a Senior Scientist with the 3M Corporation, developing some of the first models for electronic transport and optical properties of wide bandgap II–VI semiconductors, while being a Key Member of the blue laser team. He is currently the Director of the Centre for advanced nanotechnology, the Stanley Meek Chair in nanotechnology, and a Professor of applied science and engineering at the University of Toronto, Toronto, ON, Canada. His research interests include optical and transport properties of II–VI based infrared detector materials. He has published more than 260 publications in international refereed journals (with more than 4684 citations), has co-authored 4 books and has 14 patents. He is one of the Founders of a Canadian National Centre of Excellence in Photonics.

Dr. Ruda is a Fellow of the Royal Society of Canada, Fellow of Institute of Physics, and Fellow of the Institute of Nanotechnology.

Francis P. Dawson (S'86–M'87–F'09) received the B.Sc. degree in physics, and the B.ASc., M.A.Sc., and Ph.D. degrees in electrical engineering from the University of Toronto, Toronto, ON, Canada, in 1978, 1982, 1985, and 1988, respectively.

From 1978 to 1980, he was a Process Control Engineer in the pulp and paper, rubber, and textile industries. From 1982 to 1984, he was a Consultant on various projects. Since 1988, he has been with the Department of Electrical and Computer Engineering, University of Toronto, where he is involved in teaching and research. His research interests include static power converters and their applications, signal processing in power engineering applications, energy storage systems, and device or process modeling. He was also a Consultant or Project Leader in several industrial projects.

Dr. Dawson is a Member of the Association of Professional Engineers of Ontario.